Measurement of the antineutron-proton cross section at low energy

B. Gunderson,* J. Learned,† J. Mapp,‡ and D. D. Reeder

Department of Physics, University of Wisconsin, Madison, Wisconsin 53706

(Received 23 September 1980)

The total and annihilation cross sections of antineutrons on protons and carbon nuclei have been measured for antineutron momenta 0.25 to 0.88 GeV/c using a novel poor-geometry transmission technique. The measured cross sections are similar to antiproton cross sections in the same energy region. The presence of higher angular momenta ($\geq P$ wave) in the annihilation is confirmed down to 0.25 GeV/c. The Glauber-Wilkin correction to the $\bar{p}d$ total cross section is verified to 20% precision in this momentum region.

I. INTRODUCTION

A strong motivation for the study of the $\bar{N}$-N cross section at low energy is the possible existence of resonances and bound states near threshold.[1,2] A sufficiently large narrow resonance could be visible in the total cross section. Structure in the low-energy antinucleon total cross section has been reported.[3] Furthermore, bound states near threshold would strongly affect the behavior of the inelastic cross section at very low momentum through their effect on the S-wave scattering length.[1] But, despite considerable experimental effort, the question of the range of the annihilation interaction at low momentum remains open.

The primary difficulty in using antiprotons to address these problems is the loss of the antiproton energy due to ionization. Not only does this energy loss limit the path length that can be obtained at a given energy, but also fluctuations in energy loss make it extremely difficult to ascertain the energy of a specific interaction.

An additional difficulty encountered in using antiprotons is the necessity of using deuterium as a neutron target in order to separate the contribution of I-spin 0 and 1. Both these difficulties can be circumvented by the use of antineutrons as projectiles.[4] Antineutrons can be obtained either directly as a result of p-nucleus collisions, or indirectly from a separated antiproton beam by charge exchange ($\bar{p}p \to \bar{n}n$). In the case of charge exchange, the $\bar{n}$ momentum can be determined from the geometry of the charge-exchange interaction. In either case, at low energy the $\bar{n}$ momentum can be accurately determined by measurement of the time of flight.

We report here the measurement of the antineutron cross sections on protons and carbon nuclei using the transmission technique in poor geometry. The antineutrons were obtained from an enriched $\bar{p}$ beam by charge exchange on polyethylene. The $\bar{n}$'s were detected in an iron-scintillator calorimeter and their momentum measured by the time of flight from the charge-exchange vertex to annihilation in the calorimeter. The inclusion of an active transmission target enabled us to correct for elastic scattering and thus to obtain the total and inelastic cross sections separately.

II. EXPERIMENTAL PROCEDURES

The experiment was performed in a 1-GeV/c single-stage separated beam at the Argonne National Laboratory.[5] A schematic representation of the apparatus showing the beam-defining counters, charge-exchange target, transmission target, and calorimeter is shown in Fig. 1. The circuit diagram which defines the principal electronic signals is shown in Fig. 2.

Counters T_1, T_2, and T_3 defined the incident antiproton beam, with T_2 serving as reference for all time-of-flight measurements. The time spectrum of beam particles in T_1 is shown in Figure 3. The (π-μ)/$\bar{p}$ ratio was reduced to $\simeq 50$ after the
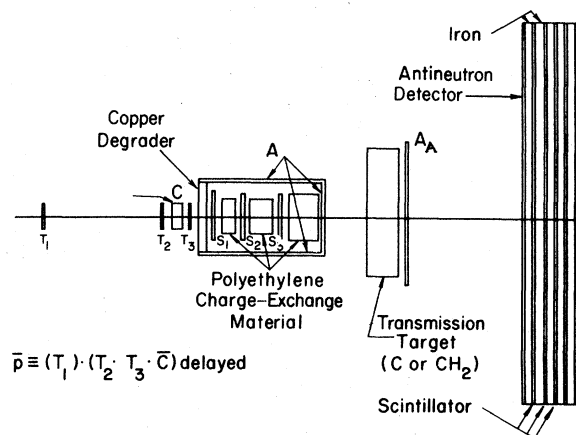

FIG. 1. Elevation view of the experimental layout (not to scale). T_1, T_2, T_3, S_1, S_2, and S_3 are scintillation counters. A and A_A are the anticoincidence scintillation counters. C is a water Cherenkov counter.
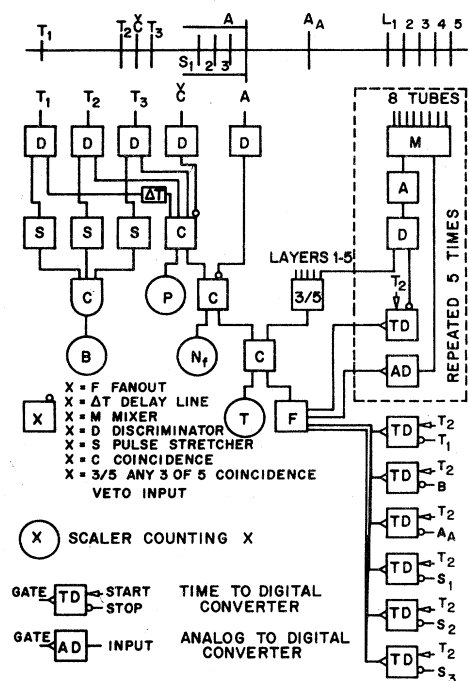
FIG. 2. Block diagram of the electronic signal processing. The counters indicated at the top of the figure are as shown in Fig. 1.

electrostatic separator. The time difference between $\bar{p}$'s and the lighter particles, together with the water Cherenkov counter in veto, enabled us to reduce the light-particle contamination of the antiproton signal in the trigger to $\lesssim 2\%$. A further selection on the time of flight at the analysis stage
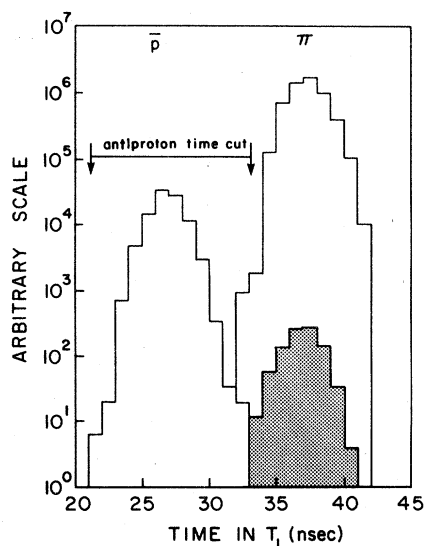

FIG. 3. Distribution of times of flight of particles in the negative beam. The shaded region shows the light-particle flux after using the water Čerenkov counter.

reduced the contamination to a negligible level. To reduce random coincidences resulting from high burst rates, we rejected events in which a second beam particle passed through T_1 within 100 μsec of a $\bar{p}$ which initiated a trigger.

The charge-exchange target was surrounded by lead-scintillator anticoincidence counters to reject annihilations and pion-charge exchange. A $\bar{p}$ signal unaccompanied by a signal in the anticounter defined an $\bar{n}$ in flight. An additional anticounter A_A, behind the transmission target, shielded the calorimeter from annihilation secondaries. A_A was not in the trigger but its time was recorded. Events having counts in A_A during the $\bar{n}$ flight to the calorimeter were rejected during the analysis. The three counters S_{1-3} localized the charge-exchange vertex to one of four target segments along the beam, thus improving the momentum resolution.

The transmission target was alternately made of carbon, or made of a heptane-based liquid scintillator with a hydrogen/carbon ratio of 2.115. The carbon target was a 60 cm $\times$ 60 cm $\times$ cm $\times$ 7 cm stack of machined graphite blocks in a retaining framework. For target-empty or heptane-target data taking this was replaced by an identical framework without the carbon.

Directly behind the carbon framework was the heptane target, a 60 cm $\times$ 60 cm $\times$ 20 cm tank with glass side walls. The heptane was viewed by eight 58 DVP phototubes, whose pulse heights and times were recorded for each event. The beam windows were constructed of aluminum sheets and honeycomb. This design resulted in low mass (0.45 g/cm^2), while providing sufficient rigidity to prevent deformation of the tank when filled with the scintillator. For empty-target or carbon-target data taking, the heptane was drained into a reservoir below the target.

Table I gives the target parameters used in the calculation of the cross section. The formula for the absorption cross section is

$$\sigma_a = \sigma_{0a} \ln(F_{ia}/F_{ta}) \,,$$

where

$$\sigma_{0a} = \frac{M_a}{N_0 \rho_a L_a} \,.$$

Here N_0 is Avogadro's number and M_a, ρ_a, and L_a are the molecular weight, target density, and target length, respectively for target a. The length is adjusted to account for beam divergence (about 1.5%). F_{ia} and F_{ta} are the incident and transmitted antineutron fluxes for target a.

The calorimeter consisted of five scintillator planes 1.8 m square interleaved with 2.5-cm iron

TABLE I. The parameters of the several attenuation targets.

Target type a	Density ρ_a (g/cm^3)	Length L_a (in.)	Molecular weight M_a (g)	σ_{0a} (mb)
Carbon	1.74 ± 0.02	2.77 ± 0.002	12.0115	1627 ± 19
Heptane	0.708	8.00 ± 0.03	14.1430	1632 ± 6

plates for a total thickness of ~ 1 absorption length. An $\bar{n}$-in-flight signal, which was followed within 100 nsec by a threefold, fourfold, or fivefold co-incidence of the calorimeter-scintillator signals, produced a trigger. Pulse height as well as time relative to T_2 was recorded for each scintillator plane in order to correct for time slewing. All counters were gated off during data recording so that no dead-time corrections were necessary.

The times of all planes corrected for pulse height were averaged to obtain the time of flight. If the rms deviation of the average exceeded 4.0 nsec, the time most in disagreement with the average was discarded and the mean recalculated. This occurred in less than 10% of the events. The time spectrum of events originating in each segment of the charge-exchange target showed a clear peak characteristic of the $\bar{n}$ momentum spectrum produced by that segment. The effect of accidental coincidences was reduced by rejecting events whose times were outside these peaks.

In Fig. 4(a) we show the time spectrum of beam muons in one calorimeter plane; the full width at half height is 5.5 nsec. Since the muons were confined to a relatively small area near the beam axis, this represents the intrinsic resolution of our electronics. The averaging procedure im-proves the time resolution for antineutrons by $\sqrt{3}$ to $\sqrt{5}$ depending on the number of planes averaged. The antineutrons were spread uniformly over the entire calorimeter. The calorimeter counters were split into quarters, each viewed from only one side. Uncertainty in the position of the anni-hilation across the calorimeter resulted in a de-gradation of the time resolution which had a stan-dard deviation of 2.42 nsec.

In Fig. 4(b) we show the relation of the time resolution to momentum resolution. At high en-ergy the momentum resolution is poor, exceeding 15% above about 500 MeV/c. However, in the normally difficult region below 300 MeV/c even our modest time resolution gives a good momen-tum measurement; the uncertainty at 250 MeV/c is ± 12.5 MeV/c.

In Fig. 5 we show the spectrum of momenta mea-sured by time of flight for antineutrons detected in the calorimeter with the dummy transmission target. The effect of time resolution is particular-

ly noticeable at the upper end where we expect a sharp kinematic cutoff at about 1 GeV/c. The re-sults of a Monte Carlo calculation of the $\bar{n}$-mo-mentum spectrum are also shown. From the agreement of Monte Carlo and data we conclude that we can correctly describe the characteristics of the antineutrons coming from the charge-ex-change target, which are important for the elastic-scattering calculation.

As mentioned above, we can also determine the $\bar{n}$ momentum from the geometry of the charge-ex-change reaction. For momenta that are large compared to the n-p mass difference, the kine-matics of $\bar{p}p$ charge exchange is the same as for $\bar{p}p$ elastic scattering. Our calorimeter subtrends a small solid angle (~ $0.02 \times 4\pi$) in the forward direction. The kinematics then requires that an $\bar{n}$, to be detected, must have a momentum nearly
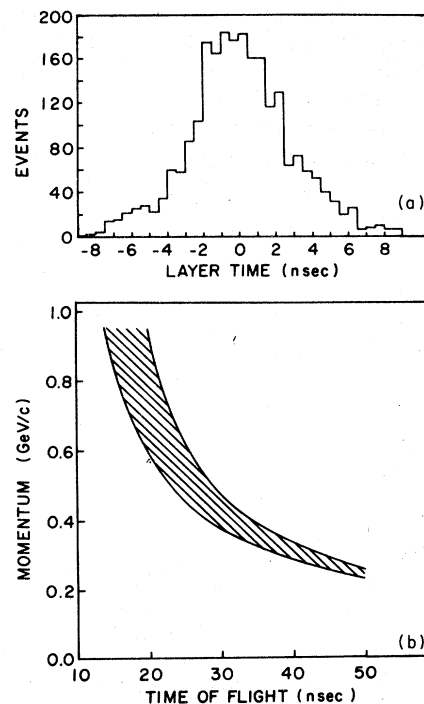

FIG. 4. (a) The distribution of the arrival times of beam muons as measured in one layer of the calorimeter detector. (b) The relation of time of flight to antineutron momentum. The shaded region shows the effect of time resolution on the momentum resolution.
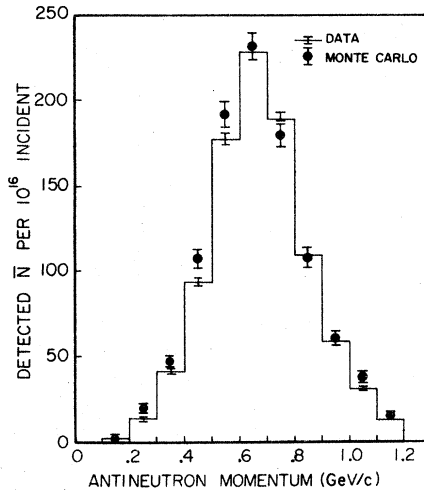
FIG. 5. The momentum spectrum of the antineutron beam measured with an empty target.

equal to that of the $\bar{p}$ which produced it. This, combined with the well-defined ionization-energy loss for a $\bar{p}$ whose momentum exceeds 300 MeV/c, means that the $\bar{n}$-momentum spectrum from each of the first three target segments should be sharply defined. This effect is clearly seen in the Monte Carlo results shown in Fig. 6. Thus, we need not use the time of flight for events originating from the first three target segments except in selecting the final event sample.
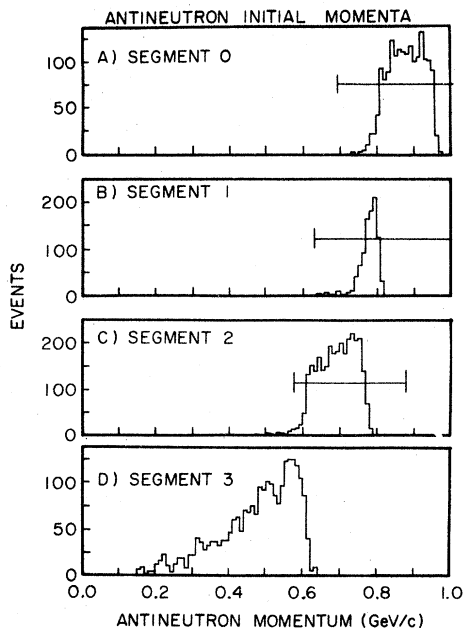

FIG. 6. The results of a Monte Carlo calculation of the momenta of the antineutrons which are made in various segments of the charge-exchange target.

The fluxes have been corrected for observed phototube gain fluctuations which were correlated among all tubes in the experiment. Since the high voltage supplied to all tubes was carefully monitored, we believe these fluctuations were caused by occasional large temperature variations in the experimental hall. The average correction was ~3%, although the correction was occasionally as large as 15%. The systematic error due to this fluctuation was estimated using the spread among rates from different runs.

Background events which escaped the beam-counter and anticoincidence counter time cuts can be seen in the time-of-flight spectra outside the peaks for the four charge-exchange target segments. The correction to the cross section for this random background was estimated from these events to be less than 2%.

The largest correction to the cross section arises from elastic scattering. A Monte Carlo simulation was used to calculate the fraction of the incident antineutron flux scattered out of the calorimeter by $\bar{n}p$ and $\bar{n}C$ elastic scattering. Direct measurements of the $\bar{p}n$ elastic cross section (in deuterium) were used in the calculation.[6-10] An optical model was used to parametrize the nC diffractive-scattering cross section.[11]

The latter process could in principle be significantly modified by the quasielastic scattering of the antineutron by a nucleon inside the nucleus. We can estimate the size of this effect by using the fact that $\bar{p}C$ charge exchange is 35% of $\bar{p}p$ charge exchange at 1 GeV/c incident-$\bar{p}$ momentum.[12] Assuming the same ratio for quasielastic scattering and using I-spin invariance, the $\bar{n}C$ quasielastic cross section is 50 mb nucleus at 500 MeV/c. That is, it is about 15% of the $\bar{n}C$ diffractive cross section.

Furthermore, the angular distribution of $\bar{n}C$ quasielastic scattering is expected to be similar to the diffraction distribution and not related to the $\bar{n}p$ elastic-scattering distribution. This is a result of the large absorption cross section which restricts the quasielastic process to those nucleons on the periphery of the nucleus.

In summary, the inclusion of quasielastic scattering will not change the angular distribution of the carbon diffraction scattering but may increase the cross section in magnitude by ~15%.

Because the carbon target subtended a slightly larger solid angle than the calorimeter, elastic scattering from the carbon target would affect the number of detected antineutrons both by inscattering and outscattering. The angular distribution of the $\bar{n}C$ elastic scattering cross section is sharply forward peaked, so that this mismatch resulted in a small net correction to the carbon cross section.

TABLE II. Corrections to the cross-section calculation due to elastic scattering in the transmisssion targets.

$P_{\bar{n}}$ (GeV/c)	$\Delta\sigma_{abs}(\bar{n}C)$ (mb)	$P_{\bar{n}}$ (GeV/c)	$\Delta\sigma_{abs}(\bar{n}p)$ (mb)	$\Delta\sigma_{tot}(\bar{n})$ (mb)
0.88	-0 ± 1	0.88	-20 ± 2	$+25 \pm 3$
0.73	-10 ± 2	0.73	-49 ± 5	$+23 \pm 3$
0.50	-7 ± 2	0.55	-63 ± 6	$+17 \pm 2$
0.30	-7 ± 2	0.45	-63 ± 6	$+17 \pm 2$
		0.35	-63 ± 6	$+17 \pm 2$
		0.25	-63 ± 6	$+17 \pm 2$

The solid angle subtended by the heptane target matched exactly the solid angle subtended by the calorimeter; thus only outscattering occurred. The more uniform angular distribution of anti-neutron-proton elastic scattering, assumed to be the same as antiproton-proton elastic scattering, then resulted in a significant correction to the heptane data.

The corrections to the cross section as calculated by the Monte Carlo simulation are given in Table II. The errors are estimated from the systematic and statistical accuracy of the Monte Carlo calculation.

We can further test the assumptions used in Monte Carlo calculation by comparing the pulse-height distribution observed in the heptane target to the recoil proton kinetic-energy spectrum predicted by the Monte Carlo calculation. Although scattering from both carbon and hydrogen occurs, very little energy is transferred to the nucleus, so that all the energy deposited in the heptane can be attributed to the recoil proton from $\bar{n}p$ elastic scattering.

In order to verify this supposition, we scanned a sample of pictures obtained by exposing a pro-pane-filled bubble chamber to a low-energy (800-MeV) antiproton beam.[13] One-pronged and two-pronged elastic scatters were observed and the scattering angle and momentum of the antiproton were recorded. The recoil proton from $\bar{p}p$ elastic scatters was easily seen (two prongs), whereas the recoil carbon was stopped without making a visible track (one prong).

The fraction of antiprotons entering the chamber and scattering elastically from the hydrogen (carbon) is calculated, using measured cross sections, to be 5.7% (8.8%).[14] The values found in the scanning were $(5.7 \pm 0.5)\%$ for hydrogen and $(9.4 \pm 0.8)\%$ for carbon.

In addition to the agreement in magnitude, the angular distributions also corroborate the assignment of one prong to $\bar{p}C$ scattering and two prongs to $\bar{p}p$ scattering. In Fig. 7 we plot the experimental distributions in momentum transfer for the two categories. The distribution for one-pronged events is sharply peaked ($\sim e^{46t}$) in satisfactory agreement with the distribution expected for diffraction scattering from carbon, viz., $e^{R^2 t/2}$, where R is the nuclear radius. For the two-pronged events the distribution is less peaked. We observe $dN/dt \sim e^{16t}$ to be compared with the previously measured value $\sim e^{17t}$.[15]

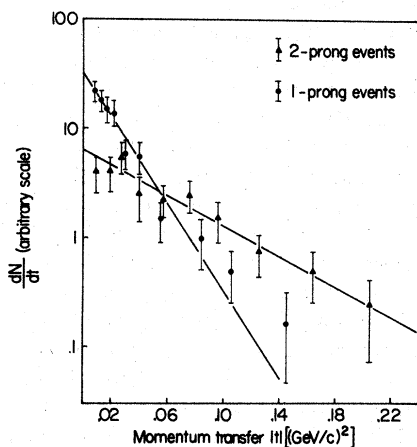The heptane-target pulse height was calibrated to an energy scale using the muons in the beam.

FIG. 7. The momentum-transfer distribution of anti-protons scattering from propane. The line through the one-pronged (two-pronged) event distribution is $\sim e^{16t}$ (e^{48t}).
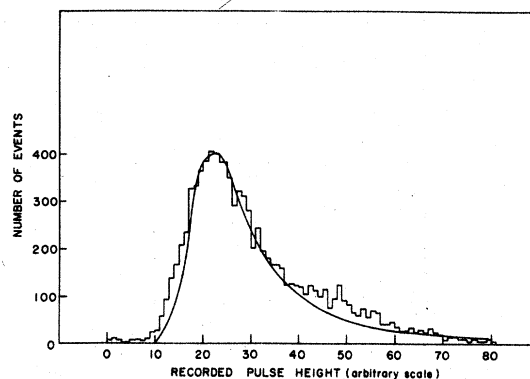

FIG. 8. The pulse-height spectrum of muons as measured in the active transmission target (heptane).
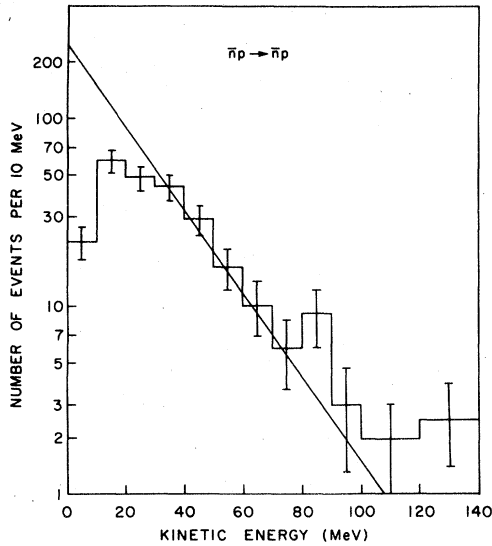
FIG. 9. The kinetic-energy spectrum of the recoil protons resulting from $\bar{n}p$ elastic scattering in the active transmission target (heptane). The solid line is the expected distribution normalized to the total number of antineutrons incident on the heptane target.

The energy loss of a 1-GeV/c muon per g/cm^2 in heptane is 31.6 MeV. In Fig. 8 we show the heptane pulse-height spectrum for muons with the mean scaled to 31.6 MeV. The shape is consistent with the expected Landau energy-loss distribution. About half the width of the distribution can be attributed to physical fluctuations in the energy loss and to photoelectron statistics, and the remainder to the photomultiplier-gain instabilities mentioned previously.

In Fig. 9 are shown the heptane data and the Monte Carlo prediction normalized to the total number of incident antineutrons. The agreement from 30 to 90 MeV is excellent, verifying both the magnitude and angular dependence of our assummed $\bar{n}p$ elastic-scattering cross section. The decrease in the observed energy spectrum below 30 MeV is due to the time requirement put on heptane pulses to remove random pulses; very small

pulses failed to trigger the discriminator which in turn stopped the clock.

The small excess of events above 80 MeV, $\sim 5\%$ of the total expected rate, is due to contamination of the pulse-height data with annihilation events. There is an enhancement at very short times which is visible in the calorimeter time spectrum for events with pulses in the heptane. This is attributed to annihilation secondaries which are recorded in the calorimeter. Most of these events can be eliminated because they are inconsistent with the time of flight expected for the four charge-exchange target segments. The number estimated to survive these cuts agrees with the observed number of large-pulse-height events.

III. DISCUSSION OF RESULTS

Our final results for the cross sections are given in Table III, the errors quoted include both statistical and systematic effects. The $\bar{n}p$ total cross section is plotted in Fig. 10 along with a previous measurement by Franklin.[6] The smooth curve is a fit, to the form $A + BP_{lab}^{-1}$ ($A = 60.4$ mb, $B = 55.4$ mb GeV/c^{16} obtained using the $\bar{p}p$ total cross section above 500 MeV/c. Clearly the $\bar{n}p$ total cross section is well represented by this curve. The equality of $\bar{p}p$ and $\bar{n}p$ total cross sections implies that the $\bar{N}$-N interactions proceed equally strongly in $I = 0$ and $I = 1$ states as corroborated by the small value of the $\bar{p}p$ charge-exchange crosssection. It should be noted that this is among the first direct checks of this equality in this energy range which does not rely on nuclear-shadowing corrections.

The $\bar{n}p$ annihilation cross section is shown in Fig. 11, together with higher-energy $\bar{p}n$[7] data and an early measurement of $\bar{p}p$ annihilation[17] in this region. The $\bar{n}$ data are consistent with the earlier measurements in other initial states. The cross-section increases slowly down to ~ 350 MeV/c below which there is an abrupt rise, the cross section remaining above the S-wave unitarity bound indicated by the lower solid line. This behavior

TABLE III. The values of the absorption cross section for antineutrons on carbon and hydrogen and the antineutron-proton total cross section obtained at various antineutron momenta.

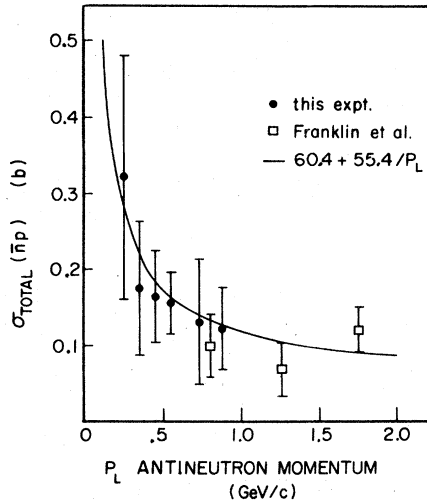| $P_{\bar{n}}$ (GeV/c)	σ_{abs} ($\bar{n}$C)	$P_{\bar{n}}$ (GeV/c)	σ_{tot} ($\bar{n}p$)	σ_{abs} ($\bar{n}p$)
0.88	418 $\pm$ 93	0.88	121 $\pm$ 53	76 $\pm$ 53
0.73	435 $\pm$ 140	0.73	132 $\pm$ 82	80 $\pm$ 82
0.50	465 $\pm$ 121	0.55	155 $\pm$ 43	75 $\pm$ 44
0.30	398 $\pm$ 280	0.45	164 $\pm$ 59	84 $\pm$ 60
		0.35	175 $\pm$ 86	95 $\pm$ 85
		0.25	323 $\pm$ 156	243 $\pm$ 156

FIG. 10. The antineutron-proton total cross section as measured in this experiment together with the measurements of Franklin *et al.* (Ref. 6).

was previously noted by Cline *et al.*[18] in a bubble-chamber experiment. Loken and Derrick[17] have suggested that an absorbing core of radius 0.87 fm in the meson cloud would produce an annihilation cross section which describes the data below pion-production threshold quite well.

In Fig. 12 we show the $\bar{n}C$ annihilation cross section together with the antiproton data of Abrams *et al.*,[11] and with the prediction of the optical model used in the Monte Carlo. Our results join smoothly to the previous measurements.
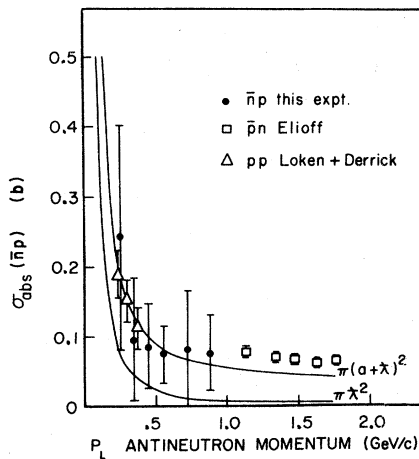
FIG. 11. The antineutron-proton absorption cross section as measured in this experiment. The lower curve is the S-wave unitarity limit and the upper curve has $a = 0.87$ fm.
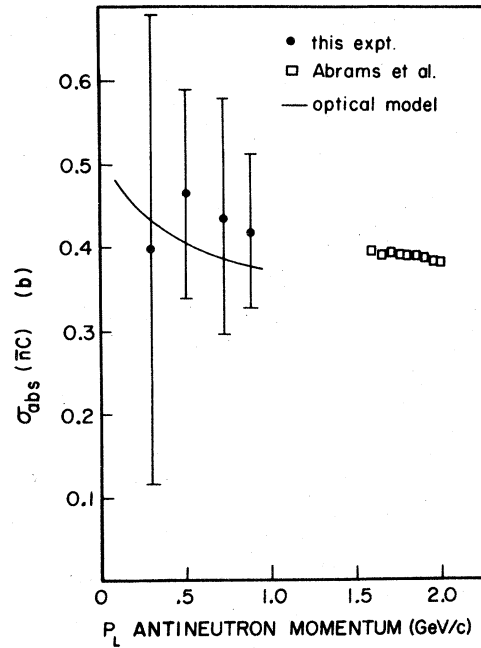

FIG. 12. The antineutron-carbon absorption cross section as measured in this experiment.

IV. SUMMARY OF CONCLUSIONS

The authors view this experiment as a first attempt to utilize a new technique for investigating low-energy $\bar{N}$-N systems. As such it was successful in that the technique has been proven and we have learned how to improve it. It is clearly necessary to control the experimental conditions more closely than we were able to do; however, this is not a fundamental problem. The major difficulties encountered in extending these measurements to lower momentum were the high rate of unwanted particles in the beam and the small solid angle of the antineutron detector. A more sophisticated apparatus in a purer $\bar{p}$ beam has great promise as a tool for investigating the threshold region of the $\bar{N}$-N system.

ACKNOWLEDGMENTS

*Present address: Max Planck Institute for Physics and Astrophysics, Munich, Germany.

†Present address: University of California, Irvine, California.

‡Present address: 1972 Commonwealth Avenue, Madison, Wisconsin 53711.

[1]J. L. Rosner, in *New Directions in Hadron Spectroscopy*, proceedings of the Summer Symposium, Argonne, Illinois, 1975, edited by S. L. Kramer and E. L. Berger (ANL, Argonne, 1975), p. 165.

[2]C. B. Dover, BNL Report No. 20148, 1975 (unpublished).

[3]A. S. Carrol *et al.*, Phys. Rev. Lett. 32, 247 (1974).

[4]An alternative method which uses the rf timing of the primary proton beam at the Alternating Gradient Synchrotron to measure $\bar{n}$ momentum has been proposed by T. Kalogeropoulos *et al.*, E-626 at the Brookhaven National Laboratory (unpublished).

[5]E. Colton, ANL Report No. EC-3, 1975 (unpublished).

[6]A. D. Franklin and R. R. Socash, Phys. Rev. 184, 1413 (1969).

[7]T. Elioff *et al.*, Phys. Rev. 128, 869 (1962).

[8]E. Bracci *et al.*, CERN Report No. CERN/HERA 73-1, 75, 1973 (unpublished).

[9]V. Scherer, Ph.D. thesis, University of Wisconsin, 1974 (unpublished).

[10]J. E. Enstrom *et al.*, LBL Report No. LBL-58, 1972 (unpublished).

[11]R. J. Abrams *et al.*, Phys. Rev. D 4, 3235 (1971).

[12]J. Button, T. Elioff, T. Segre, H. M. Steiner, R. Weingart, C. Wiegand, and T. Ypsilantis, Phys. Rev. 108, 1557 (1957).

[13]The film was made available by the Argonne National Laboratory.

[14]The values of the elastic-scattering cross sections used in the calculations were 55 mb for $\bar{n}p$ and 225 mb for $\bar{n}C$ elastic scattering. Data can be obtained from E. Bracci *et al.*, CERN Report No. CERN/HERA 73-1, (unpublished); W. A. Wenzel, in *Proceedings of the 1960 Annual International Conference on High Energy Physics*, edited by E. C. G. Sudershan, J. H. Tinlot, and A. C. Melissinos (University of Rochester, Rochester, N.Y., 1960), p. 151; Ref. 11.

[15]R. Armenteros and B. French, *High Energy Physics*, edited by E. H. S. Burhop (Academic, New York, 1969), Vol. IV, p. 287.

[16]T. Kalogeropoulos, in *Experimental Meson Spectroscopy—1974*, Proceedings of the Fourth International Conference, Boston, edited by D. Garelick (AIP, New York, 1974) p. 97.

[17]J. G. Loken and M. Derrick, Phys. Lett. 3, 334 (1963).

[18]D. Cline *et al.*, Phys. Rev. Lett. 27, 71 (1971).